

Ti₃C₂T_x/MoS₂ Self-Rolling Rod-Based Foam Boosts Interfacial Polarization for Electromagnetic Wave Absorption

Minghang Li, Wenjie Zhu, Xin Li, Hailong Xu, Xiaomeng Fan,* Hongjing Wu,* Fang Ye, Jimei Xue, Xiaoqiang Li, Laifei Cheng, and Litong Zhang

Heterogeneous interface design to boost interfacial polarization has become a feasible way to realize high electromagnetic wave absorbing (EMA) performance of dielectric materials. However, interfacial polarization in simple structures such as particles, rods, and flakes is weak and usually plays a secondary role. In order to enhance the interfacial polarization and simultaneously reduce the electronic conductivity to avoid reflection of electromagnetic wave, a more rational geometric structure for dielectric materials is desired. Herein, a Ti₃C₂T_x/MoS₂ self-rolling rod-based foam is proposed to realize excellent interfacial polarization and achieve high EMA performance at ultralow density. Different surface tensions of Ti₃C₂T_x and ammonium tetrathiomolybdate are utilized to induce the self-rolling of Ti₃C₂T_x sheets. The rods with a high aspect ratio not only remarkably improve the polarization loss but also are beneficial to the construction of Ti₃C₂T_x/MoS₂ foam, leading to enhanced EMA capability. As a result, the effective absorption bandwidth of Ti₃C₂T_x/MoS₂ foam covers the whole X band (8.2–12.4 GHz) with a density of only 0.009 g cm⁻³, at a thickness of 3.3 mm. The advantages of rod structures are verified through simulations in the CST microwave studio. This work inspires the rational geometric design of micro/nanostructures for new-generation EMA materials.

1. Introduction

Spatial electromagnetic (EM) wave pollution has been an unavoidable issue in daily life with the rapid development of electronic technology. To reduce EM wave interference, extensive studies about EM wave absorbing (EMA) materials have been propelled.^[1] Generally, the rational design of heterogeneous interface in dielectric EMA materials can optimize the impedance match conditions (Table S1, Supporting Information).^[2] As a result, the optimal heterogeneous interface design has become a mainstream way to realize high EMA performance.^[3]


2D material Ti₃C₂T_x MXene is often used to carry on interface design due to its high specific surface areas and solution-processibility.^[4] However, the pristine Ti₃C₂T_x possesses high electrical conductivity (higher than 10 000 S cm⁻¹), leading to impedance mismatch and showing EM interference (EMI) shielding performance.^[5] For instance, Ti₃C₂T_x foam with a density of 5.5 mg cm⁻³ shows shielding

effectiveness of 54.8 dB.^[6] To optimize the impedance match condition, heterogeneous interface design based on Ti₃C₂T_x has been carried out, such as Ti₃C₂T_x/SiC, Ti₃C₂T_x/NiCo₂O₄, and so on.^[7] Although the EMA performances have been improved to some extent in these structures, the interfacial polarizations are still weak in these traditional sheet structures. Due to the limit of sheet structures, it is hard to increase the number of interfaces between two sheets. Recent research verifies that the rod structure is one of the most effective structures to enhance polarization loss, such as core-shell or core-sheath.^[8] Nevertheless, in these structures, the interface structure between core and shell is very simple. Self-rolling rod structures without cores are expected to overcome the above problems and realize the great increase of interfaces between two materials. The interfaces between two materials will increase greatly with the decrease of the diameter of this self-rolling rod structure. Furthermore, the electronic conductivity of Ti₃C₂T_x will decrease rapidly due to the composition with the second phase such as semiconductor in the self-rolling rod structure, which could optimize the impedance match conditions. However, there are still synthetic methodological challenges to the implementation of self-rolling rod structures for Ti₃C₂T_x.

M. Li, W. Zhu, X. Li, X. Fan, F. Ye, J. Xue, X. Li, L. Cheng, L. Zhang
Science and Technology on Thermostructural Composite Materials
Laboratory
Northwestern Polytechnical University
Xi'an 710072, P. R. China
E-mail: fanxiaomeng@nwpu.edu.cn

H. Xu
Institute of Textiles and Clothing
The Hong Kong Polytechnic University
Hong Kong SAR 999077, P. R. China

H. Wu
MOE Key Laboratory of Material Physics and Chemistry under
Extraordinary School of Physical Science and Technology
Northwestern Polytechnical University
Xi'an 710072, P. R. China
E-mail: wuhongjing@nwpu.edu.cn

 The ORCID identification number(s) for the author(s) of this article can be found under <https://doi.org/10.1002/advs.202201118>

© 2022 The Authors. Advanced Science published by Wiley-VCH GmbH. This is an open access article under the terms of the Creative Commons Attribution License, which permits use, distribution and reproduction in any medium, provided the original work is properly cited.

DOI: 10.1002/advs.202201118

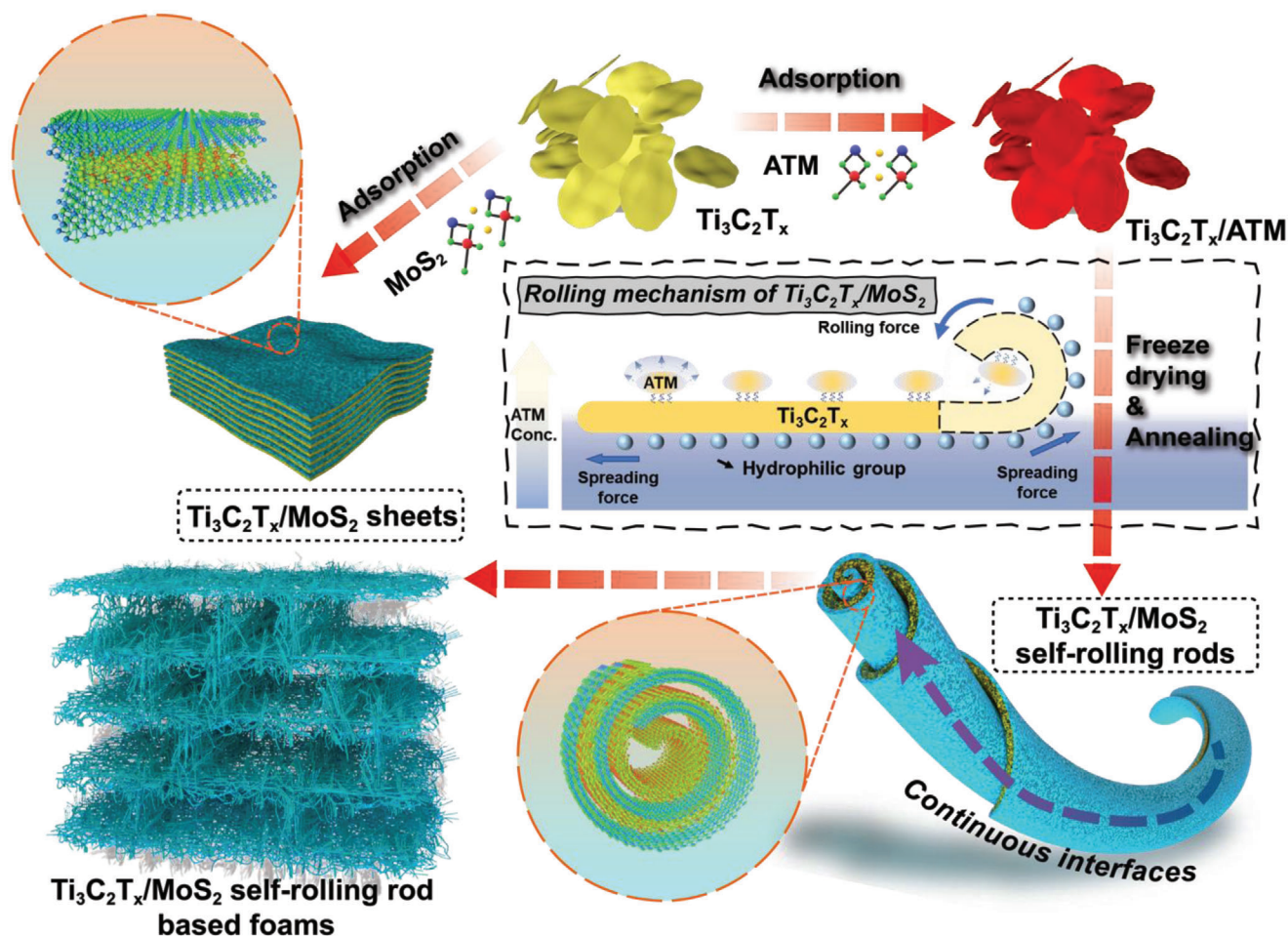


Figure 1. Schematic illustration of the fabrication process of $\text{Ti}_3\text{C}_2\text{T}_x/\text{MoS}_2$ sheets and self-rolling rods and rolling mechanism of $\text{Ti}_3\text{C}_2\text{T}_x/\text{MoS}_2$ self-rolling rods.

Except for microstructure, macroscopic foam structures are usually adopted as one of the most promising structures for EMA materials, whose high porosity facilitates the entry and transmission of EM wave inside samples and is beneficial to the dissipation of EM wave energy.^[1b,8,9] Self-rolling rod structures with a high aspect ratio are expected to efficiently construct EMA foams, due to the formation of intertwined networks during the process of the freeze-drying method.^[10] Therefore, self-rolling rod structures are not only helpful for constructing foam structures but also good for the formation of massive heterogeneous interfaces between two phases. Based on the above analysis, it is an efficient way to realize lightweight and high EMA capability by constructing MXene-based foam with self-rolling rod structures.

In this work, the 3D foams composed of $\text{Ti}_3\text{C}_2\text{T}_x/\text{MoS}_2$ self-rolling rods were prepared through the unidirectional freeze-drying method (Figure 1). Ammonium tetrathiomolybdate (ATM) was used as the precursor of MoS_2 . The different surface tension directions of ATM and $\text{Ti}_3\text{C}_2\text{T}_x$ would induce the self-rolling of $\text{Ti}_3\text{C}_2\text{T}_x/\text{MoS}_2$.^[11] There is a big jump in the number of interfaces after the self-rolling process and the interfaces between $\text{Ti}_3\text{C}_2\text{T}_x$ and MoS_2 are utilized to increase the interfacial polarization. As a result, the ratio of polarization loss

remarkably reaches above 80% and the impedance match condition is greatly improved. The effective absorption bandwidth (EAB) covers the whole X band and can cover C and Ku bands according to simulation results. To investigate the influence of the ratio of $\text{Ti}_3\text{C}_2\text{T}_x/\text{MoS}_2$, three $\text{Ti}_3\text{C}_2\text{T}_x/\text{MoS}_2$ self-rolling rod samples named S1–S3 were prepared by adjusting the contents of $\text{Ti}_3\text{C}_2\text{T}_x$ and MoS_2 . The EMA mechanisms of $\text{Ti}_3\text{C}_2\text{T}_x/\text{MoS}_2$ self-rolling rod structures are studied through simulation in the CST microwave studio.

2. Results and Discussion

2.1. Formation Mechanism and Micro/Nanostructure

Figure 1 illustrates the fabrication process and rolling mechanism of $\text{Ti}_3\text{C}_2\text{T}_x/\text{MoS}_2$ foam. $\text{Ti}_3\text{C}_2\text{T}_x$ sheets were prepared through in situ fluohydric acid (HF) etching and hand-shaking method.^[4c] The abundant surface groups (–F, –O, and –OH) on the $\text{Ti}_3\text{C}_2\text{T}_x$ sheets make them good dispersion properties in an aqueous solution.^[12] Thus, the surface tension of $\text{Ti}_3\text{C}_2\text{T}_x$ sheets tends to flatten themselves (spreading force). However, the dispersion property of the ATM in the aqueous solution is poor. The

surface tension of ATM tends to curl the droplets from the edge to achieve minimum surface energy (rolling force).^[11b] As a result, after attachment with $\text{Ti}_3\text{C}_2\text{T}_x$ through Van der Waals' force, the rolling force derived from the surface tension of ATM would induce the self-rolling of $\text{Ti}_3\text{C}_2\text{T}_x$ sheets (Figure 1 and Figure S1, Supporting Information). Figure S2 in the Supporting Information shows that a change in pH value does not result in morphological changes of $\text{Ti}_3\text{C}_2\text{T}_x$ sheets, further proving that the surface tension is critical to the rolling of $\text{Ti}_3\text{C}_2\text{T}_x$. In addition, a temperature gradient existed along the vertical direction, benefiting from the fine control of the freezing process. While the aqueous suspension was frozen, the ice crystals grew along the vertical direction and expelled $\text{Ti}_3\text{C}_2\text{T}_x/\text{ATM}$ rod to the gaps between ice crystals. The orderly lamellar foam structure was constructed after the ice sublimation under vacuum. After annealing at 350 °C for 2 h, the MoS_2 was formed by the decomposition of the ATM. The thermogravimetry (TG) curve and decomposition equations of ATM are given in Figure S3 in the Supporting Information, which indicates that about 25% of weight loss during annealing, caused by the escape of NH_3 .^[13] To demonstrate the advantages of self-rolling rod structure, the $\text{Ti}_3\text{C}_2\text{T}_x/\text{MoS}_2$ sheets were also prepared. The ATM was annealed at first to obtain MoS_2 and then mixed with $\text{Ti}_3\text{C}_2\text{T}_x$ followed by the same unidirectional freezing process.

Figure 2a shows the X-ray diffraction (XRD) patterns of MoS_2 , $\text{Ti}_3\text{C}_2\text{T}_x$, and $\text{Ti}_3\text{C}_2\text{T}_x/\text{MoS}_2$. For the MoS_2 , the peak around 15° represents the (002) crystal plane of MoS_2 , which verifies the decomposition of ATM.^[14] The peak at 7.4° is the characteristic peak of $\text{Ti}_3\text{C}_2\text{T}_x$, representing the (002) plane of $\text{Ti}_3\text{C}_2\text{T}_x$.^[15] After heat-treatment of the $\text{Ti}_3\text{C}_2\text{T}_x$ -ATM sample, the characteristic diffraction peaks of MoS_2 appear. It is noted that the peak of the (002) plane of $\text{Ti}_3\text{C}_2\text{T}_x$ shifts from 7.4° to 6.8°, which means that the d-spacing of the (002) plane increased from 11.70 to 12.97 Å, which is consistent with the interlayer spacing of $\text{Ti}_3\text{C}_2\text{T}_x$ in Figure 3g. It can be concluded that the MoS_2 sheets were in situ formed in the interlayer of $\text{Ti}_3\text{C}_2\text{T}_x$ flakes, leading to the enlarged interlayer space. Raman spectra of MoS_2 , $\text{Ti}_3\text{C}_2\text{T}_x$, and $\text{Ti}_3\text{C}_2\text{T}_x/\text{MoS}_2$ are shown in Figure 2b. Consistent with previous studies, three broad peaks of $\text{Ti}_3\text{C}_2\text{T}_x$ are shown at ≈ 202 , 378, and 605 cm^{-1} .^[16] The broad peak at 605 cm^{-1} represents the existence of -OH groups.^[17] After binding with MoS_2 , the peak of -OH groups disappeared, which means that the ATM attaches with $\text{Ti}_3\text{C}_2\text{T}_x$ through -OH groups.

The SEM images in Figure 2c–f show that both $\text{Ti}_3\text{C}_2\text{T}_x$ and $\text{Ti}_3\text{C}_2\text{T}_x/\text{MoS}_2$ foams are similar layered structures. The layer spacing of $\text{Ti}_3\text{C}_2\text{T}_x$ foam is only 30 μm and the layer spacing of $\text{Ti}_3\text{C}_2\text{T}_x/\text{MoS}_2$ foam is 200 μm . The larger layer spacing is propitious to the entry of EM waves into $\text{Ti}_3\text{C}_2\text{T}_x/\text{MoS}_2$ foam. According to the high magnification SEM images, the layer arrangements of $\text{Ti}_3\text{C}_2\text{T}_x/\text{MoS}_2$ and $\text{Ti}_3\text{C}_2\text{T}_x$ are different. The layer of $\text{Ti}_3\text{C}_2\text{T}_x$ foam is composed of 2D $\text{Ti}_3\text{C}_2\text{T}_x$ sheets and there are some holes on the surface (Figure 2d). The layer of $\text{Ti}_3\text{C}_2\text{T}_x/\text{MoS}_2$ foam is composed of crossed rods (Figure 2f). Compared with $\text{Ti}_3\text{C}_2\text{T}_x$ and $\text{Ti}_3\text{C}_2\text{T}_x/\text{MoS}_2$ sheets, the $\text{Ti}_3\text{C}_2\text{T}_x/\text{MoS}_2$ self-rolling rods cross each other and show a rough surface (Figure 2g,h). The N_2 sorption isotherms at 77 K and pore-size distribution derived from Barrett–Joyner–Halenda method are shown in Figure S4 in the Supporting Information. The specific surface areas of $\text{Ti}_3\text{C}_2\text{T}_x/\text{MoS}_2$ sheets and $\text{Ti}_3\text{C}_2\text{T}_x/\text{MoS}_2$ self-rolling rods

are 5.2327 and 3.7463 $\text{m}^2 \text{g}^{-1}$, respectively. The self-rolling structure leads to the decrease of specific surface areas, due to a lot of surfaces being used to construct heterogeneous interfaces. The pore size distributions of $\text{Ti}_3\text{C}_2\text{T}_x/\text{MoS}_2$ sheets and $\text{Ti}_3\text{C}_2\text{T}_x/\text{MoS}_2$ self-rolling rods are similar. However, the pore volume of $\text{Ti}_3\text{C}_2\text{T}_x/\text{MoS}_2$ self-rolling rods is 0.016 $\text{cm}^3 \text{g}^{-1}$, which is higher than 0.013 $\text{cm}^3 \text{g}^{-1}$ of $\text{Ti}_3\text{C}_2\text{T}_x/\text{MoS}_2$ sheets. A larger pore volume is beneficial to the impedance match condition. To better observe the morphology of $\text{Ti}_3\text{C}_2\text{T}_x/\text{MoS}_2$ self-rolling rods, a single $\text{Ti}_3\text{C}_2\text{T}_x/\text{MoS}_2$ self-rolling rod was obtained through sonication (Figure 2j). The length of a single rod can reach tens of micrometers and there are some synapses-like structures along the rod, which are beneficial to the construction of $\text{Ti}_3\text{C}_2\text{T}_x/\text{MoS}_2$ foams. These flexible rods are interconnected through synapses (Figure S5a, Supporting Information), which are like bridges, leading to the formation of stable foam structures (Figure 2i and Figure S9, Supporting Information). The foam structures composed of $\text{Ti}_3\text{C}_2\text{T}_x/\text{MoS}_2$ self-rolling rods facilitate the entry and transmission of EM wave inside samples and are propitious to the consumption of EM wave energy through heat dissipation.^[18]

The XPS survey in Figure 2k demonstrates four main elements, including Ti, C, O, and F in $\text{Ti}_3\text{C}_2\text{T}_x$. After attaching with MoS_2 , the signal of S and Mo can be detected. The XPS spectrum of Ti 2p in pure $\text{Ti}_3\text{C}_2\text{T}_x$ foam shows four predominant peaks of Ti–O 2p_{1/2} (464.3 eV), Ti–O 2p_{3/2} (458.8 eV), Ti–C 2p_{3/2} (455.1 eV), and C–Ti–T_x 2p_{1/2} (461.1 eV) bonds. These chemical states are caused by the chemical etching process of Ti_3AlC_2 using HCl and LiF, which can introduce many functional groups.^[19] The preparation of MoS_2 is confirmed by the Mo 3d and S 2s peaks. In the S 2p spectrum, the two conspicuous peaks of S 2p_{1/2} and S 2p_{3/2} at 162.9 and 161.8 eV represent the S²⁻ of MoS_2 .^[20] It is worth noting that there is a small peak at about 169.5 eV for $\text{Ti}_3\text{C}_2\text{T}_x/\text{MoS}_2$ self-rolling rod structure, which can be assigned to S–O bonds, indicating the combination of MoS_2 and –O groups of $\text{Ti}_3\text{C}_2\text{T}_x$.^[21] The S 2p spectrum of $\text{Ti}_3\text{C}_2\text{T}_x/\text{MoS}_2$ shows that there is no S–O bond, which means MoS_2 and $\text{Ti}_3\text{C}_2\text{T}_x$ are just mixed simply. As a result, the signal of O 1s is stronger in $\text{Ti}_3\text{C}_2\text{T}_x/\text{MoS}_2$ compared with pure $\text{Ti}_3\text{C}_2\text{T}_x$ due to the partly oxidized MoS_2 layer on the surface of $\text{Ti}_3\text{C}_2\text{T}_x$.

The Raman spectra of MoS_2 show two dominant peaks around 400 cm^{-1} , which are assigned to E¹_{2g} and A_{1g} mode of S–Mo–S.^[22] The frequency difference of E¹_{2g} and A_{1g} peaks can be used to evaluate the property of MoS_2 and the distance of Mo–S bonds (Figure 3a). The frequency differences between E¹_{2g} and A_{1g} peaks are about 26 cm^{-1} for both MoS_2 and $\text{Ti}_3\text{C}_2\text{T}_x/\text{MoS}_2$ sheets, which are consistent with bulk MoS_2 .^[23] For $\text{Ti}_3\text{C}_2\text{T}_x/\text{MoS}_2$ self-rolling rods, the frequency differences between E¹_{2g} and A_{1g} peaks decrease to about 24 cm^{-1} , which are consistent with few-layer MoS_2 . Apart from that, the E¹_{2g} mode exhibits a slight blueshift from $\text{Ti}_3\text{C}_2\text{T}_x/\text{MoS}_2$ sheet to $\text{Ti}_3\text{C}_2\text{T}_x/\text{MoS}_2$ self-rolling rod, suggesting a decrease of Mo–S distance.^[24] Moreover, the A_{1g} mode exhibits an obvious redshift, which is related to the carrier doping effect, meaning the strong combination of $\text{Ti}_3\text{C}_2\text{T}_x$ and MoS_2 in self-rolling rod structure.^[17,25] All these results show that MoS_2 are formed between the layers of $\text{Ti}_3\text{C}_2\text{T}_x$, which can induce the rolling of $\text{Ti}_3\text{C}_2\text{T}_x$ sheets through a strong combination.

To directly observe the interface of $\text{Ti}_3\text{C}_2\text{T}_x$ and MoS_2 , a single $\text{Ti}_3\text{C}_2\text{T}_x/\text{MoS}_2$ self-rolling rod was chosen to prepare a cross-

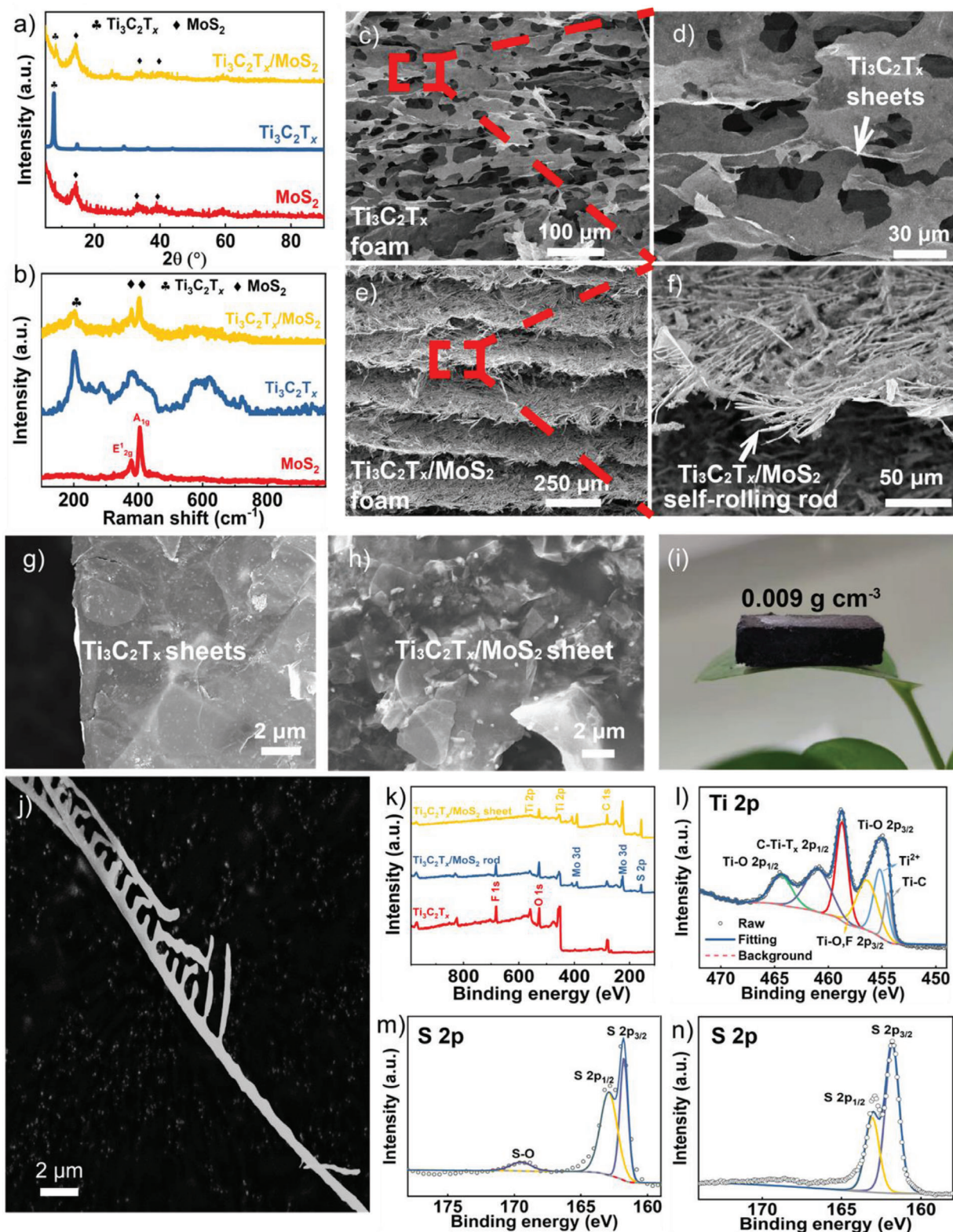


Figure 2. a) XRD and b) Raman patterns of MoS₂, Ti₃C₂T_x, and Ti₃C₂T_x/MoS₂. Cross-sectional scanning electron microscope (SEM) images of c,d) Ti₃C₂T_x foam and e,f) Ti₃C₂T_x/MoS₂ foam. SEM image of g) Ti₃C₂T_x sheets and h) Ti₃C₂T_x/MoS₂ sheets. i) The optical photos of Ti₃C₂T_x/MoS₂ self-rolling rod-based foam. j) SEM image of single Ti₃C₂T_x/MoS₂ self-rolling rod. k) X-ray photoelectron spectroscopy (XPS) spectra of Ti₃C₂T_x, Ti₃C₂T_x/MoS₂ self-rolling rod structure, and Ti₃C₂T_x/MoS₂ sheet structure. l) High-resolution of Ti 2p spectrum of Ti₃C₂T_x/MoS₂ self-rolling rod structure. m,n) High-resolution of S 2p spectrum of Ti₃C₂T_x/MoS₂ self-rolling rod structure and Ti₃C₂T_x/MoS₂ sheet structure, respectively.

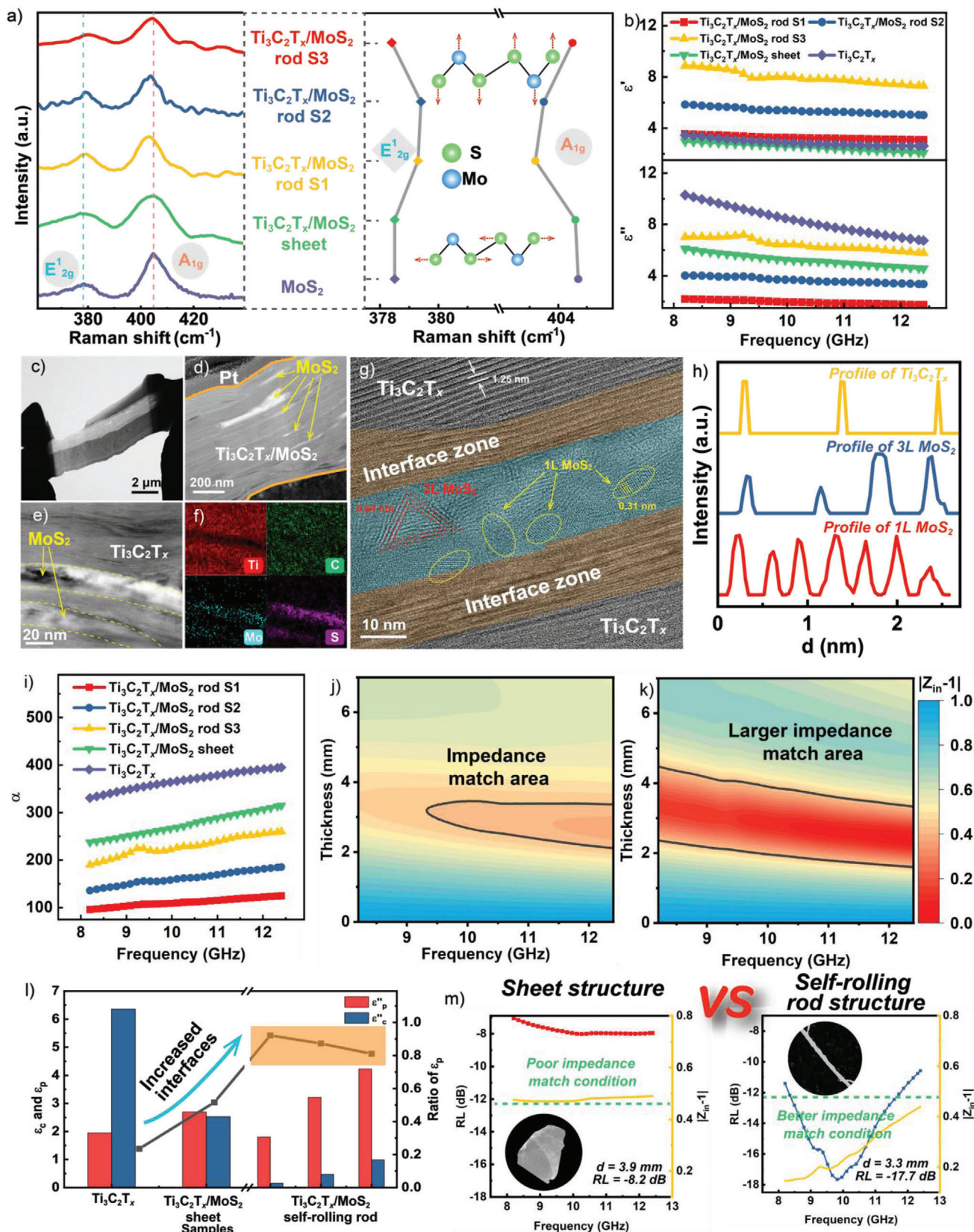


Figure 3. a) E_{2g}^1 mode and A_{1g} mode of Raman spectra of MoS_2 , $\text{Ti}_3\text{C}_2\text{T}_x/\text{MoS}_2$ sheet, and $\text{Ti}_3\text{C}_2\text{T}_x/\text{MoS}_2$ self-rolling rod. b) The real and imaginary part of permittivities of all samples. c) The cross-sectional sample of $\text{Ti}_3\text{C}_2\text{T}_x/\text{MoS}_2$ self-rolling rod prepared by FIB technique and d) its corresponding

sectional TEM sample through the focus ion beam (FIB) “lift-out” technique.^[26] A TEM sample with a length of about 8 μm was cut by FIB along the axis of the $\text{Ti}_3\text{C}_2\text{T}_x/\text{MoS}_2$ self-rolling rod (Figure 3c). The detailed preparation process is shown in Figure S10 in the Supporting Information. A typical layered structure can be seen clearly from the cross-sectional TEM image of the $\text{Ti}_3\text{C}_2\text{T}_x/\text{MoS}_2$ self-rolling rod, compared with 2D $\text{Ti}_3\text{C}_2\text{T}_x$ and 2D $\text{Ti}_3\text{C}_2\text{T}_x/\text{MoS}_2$ sheets (Figure 3d and Figures S6 and S7, Supporting Information). The MoS_2 layers alternate with $\text{Ti}_3\text{C}_2\text{T}_x$ layers with a bending feature, suggesting the rolling of $\text{Ti}_3\text{C}_2\text{T}_x/\text{MoS}_2$ (Figure 3e,f). The thickness of the MoS_2 layer is about 10 nm and there are typical triangle MoS_2 crystals with single layer property, which is consistent with the difference of E_{12g} and A_{1g} modes of $\text{Ti}_3\text{C}_2\text{T}_x/\text{MoS}_2$ self-rolling rod structures in Raman spectra (Figure 3h). An interface zone can be seen clearly between $\text{Ti}_3\text{C}_2\text{T}_x$ and MoS_2 , where can be found lattice stripes of both MoS_2 and $\text{Ti}_3\text{C}_2\text{T}_x$. This means the tight combination of $\text{Ti}_3\text{C}_2\text{T}_x$ and MoS_2 . The alternation of MoS_2 and $\text{Ti}_3\text{C}_2\text{T}_x$ would provide abundant nanoheterogeneous interfaces, which can enhance the interfacial polarization loss. The area of heterogeneous interfaces can be calculated according to the number of rolling layers of the $\text{Ti}_3\text{C}_2\text{T}_x/\text{MoS}_2$ self-rolling rod structure. In an ideal situation, it is an exponential function (Figure S11, Supporting Information). The area can be doubled at maximum, which can realize the full utilization of surface areas of $\text{Ti}_3\text{C}_2\text{T}_x$.

2.2. Electromagnetic Response Behavior and EMA Performance

The enhancement of interfacial polarization loss can influence the permittivity of corresponding samples. Generally, the ϵ' represents the ability to store charge, which is related to the multipolarizations. The ϵ'' represents the ability to attenuate EM wave energy, which is associated with both polarization loss and conductive loss. As shown in Figure 3b, the ϵ' of $\text{Ti}_3\text{C}_2\text{T}_x$ and $\text{Ti}_3\text{C}_2\text{T}_x/\text{MoS}_2$ sheets are the lowest due to weak interfacial polarization.^[27] For $\text{Ti}_3\text{C}_2\text{T}_x/\text{MoS}_2$ self-rolling rods, the ϵ' increased about two times which is corresponding to the strong interfacial polarization. As to ϵ'' , the trend is the opposite with ϵ' . The ϵ'' of $\text{Ti}_3\text{C}_2\text{T}_x$ and $\text{Ti}_3\text{C}_2\text{T}_x/\text{MoS}_2$ sheets are the highest due to high conductive loss. For $\text{Ti}_3\text{C}_2\text{T}_x/\text{MoS}_2$ self-rolling rods, the conductive network of $\text{Ti}_3\text{C}_2\text{T}_x$ would be interrupted by MoS_2 inevitably, leading to the decrease of ϵ'' . Also, the electrical conductivity decreased due to the broken conductive network (Figure S16, Supporting Information). It is noted that the ϵ'' values rise at 9–10 GHz in $\text{Ti}_3\text{C}_2\text{T}_x/\text{MoS}_2$ self-rolling rods. This is caused by the dielectric relaxation originating from interfacial polarization. The Cole-Cole circles of $\text{Ti}_3\text{C}_2\text{T}_x/\text{MoS}_2$ self-rolling rod S2 (Figure S14, Supporting Information) reveal that the polarization loss at 9–10 GHz is the strongest. Figure 3i shows the attenuation constant of all samples, which can represent the overall EM loss capacity of the material. It can be found that $\text{Ti}_3\text{C}_2\text{T}_x/\text{MoS}_2$ sheet

has a higher EM loss capacity than the $\text{Ti}_3\text{C}_2\text{T}_x/\text{MoS}_2$ self-rolling rod. However, according to Figures 3j,k, the self-rolling rod structure shows a larger impedance match area. To better understand this phenomenon, the polarization loss and conductive loss are calculated based on Debye theory (Figure 3l, detailed information is shown in the Supporting Information). The conductive loss plays a primary role in $\text{Ti}_3\text{C}_2\text{T}_x$ and $\text{Ti}_3\text{C}_2\text{T}_x/\text{MoS}_2$ sheets due to the high conductivity of $\text{Ti}_3\text{C}_2\text{T}_x$. After the rolling process, the polarization loss increases about two times and plays a primary role with a better impedance match. The better impedance condition of $\text{Ti}_3\text{C}_2\text{T}_x/\text{MoS}_2$ self-rolling rod structures leads to better EMA performance, compared with $\text{Ti}_3\text{C}_2\text{T}_x/\text{MoS}_2$ sheets in Figure 3m.

The EMA performances of these foams are evaluated by the wave-guide method, which ensures the structural integrity of the foam structures. The test direction is vertical to the layer of foams, as shown in Figure S12 in the Supporting Information. This direction maximizes the effect of the layer-by-layer structure constructed in the unidirectional freeze-drying process. Strong reflection of the EM wave caused by the highest ϵ'' makes $\text{Ti}_3\text{C}_2\text{T}_x$ foams show EMI shielding performance (Figure S13, Supporting Information). The downward trend of ϵ'' with frequency increasing agrees well with the decrease of SE_R . With the addition of MoS_2 , the EMA performances are improved substantially. The reflection loss (RL) contours of the $\text{Ti}_3\text{C}_2\text{T}_x/\text{MoS}_2$ sheet are shown in Figure 4a. The minimum reflection loss (RL_{\min}) is -8.2 dB. Although its absorption of EM wave energy reached more than 84%, the narrow absorption band still cannot meet the requirement. In contrast, when $\text{Ti}_3\text{C}_2\text{T}_x/\text{MoS}_2$ sheets are rolled into rods, the RL_{\min} can reach -52.1 dB and the EAB can cover the whole X band (Figure 4b,c). More detailed RL curves with different thicknesses are shown in Figure S15 in the Supporting Information. The corresponding frequency of RL_{\min} shifts to a lower frequency with increased thickness. This effect is caused by the quarter-wavelength model.^[28] Due to the excellent absorption of $\text{Ti}_3\text{C}_2\text{T}_x/\text{MoS}_2$ self-rolling rod-based foams at the X band, the EMA performance at 2–18 GHz was also simulated by the CST microwave studio suite based on the standard finite difference time domain method. The EAB is 6.5 GHz and can cover C, X, and Ku bands (4–18 GHz) with varied thicknesses (Figure S17, Supporting Information). The $\text{Ti}_3\text{C}_2\text{T}_x/\text{MoS}_2$ self-rolling rod-based foams can satisfy the application requirements of “thin, light, strong, and broad” for EMA materials. Certainly, the EMA performance could be further improved through tuning the properties of the self-rolling rod, such as diameters and rolling methods.

2.3. EMA Mechanism and Physical Model

To further reveal the advantage of self-rolling rod structure, the $\text{Ti}_3\text{C}_2\text{T}_x/\text{MoS}_2$ sheet structure and $\text{Ti}_3\text{C}_2\text{T}_x/\text{MoS}_2$ self-rolling rod

transmission electron microscope (TEM) images. e,f) The high-magnification TEM image and its corresponding energy disperse spectroscopy (EDS) mapping images. g) The interface between $\text{Ti}_3\text{C}_2\text{T}_x$ and MoS_2 . h) The intensity profiles of 1L MoS_2 , 3L MoS_2 , and $\text{Ti}_3\text{C}_2\text{T}_x$. i) Attenuation constants of $\text{Ti}_3\text{C}_2\text{T}_x$, $\text{Ti}_3\text{C}_2\text{T}_x/\text{MoS}_2$ sheets, and $\text{Ti}_3\text{C}_2\text{T}_x/\text{MoS}_2$ self-rolling rods. $|Z_{\text{in}} - 1|$ contours of j) $\text{Ti}_3\text{C}_2\text{T}_x/\text{MoS}_2$ sheets and k) $\text{Ti}_3\text{C}_2\text{T}_x/\text{MoS}_2$ self-rolling rods. l) The conductive and polarization loss of $\text{Ti}_3\text{C}_2\text{T}_x$, $\text{Ti}_3\text{C}_2\text{T}_x/\text{MoS}_2$ sheets, and $\text{Ti}_3\text{C}_2\text{T}_x/\text{MoS}_2$ self-rolling rods. m) Comparison of EMA performances for $\text{Ti}_3\text{C}_2\text{T}_x/\text{MoS}_2$ sheets and $\text{Ti}_3\text{C}_2\text{T}_x/\text{MoS}_2$ self-rolling rods, revealing the superiority of self-rolling rod structure for enhancing EM wave absorption and impedance match condition.

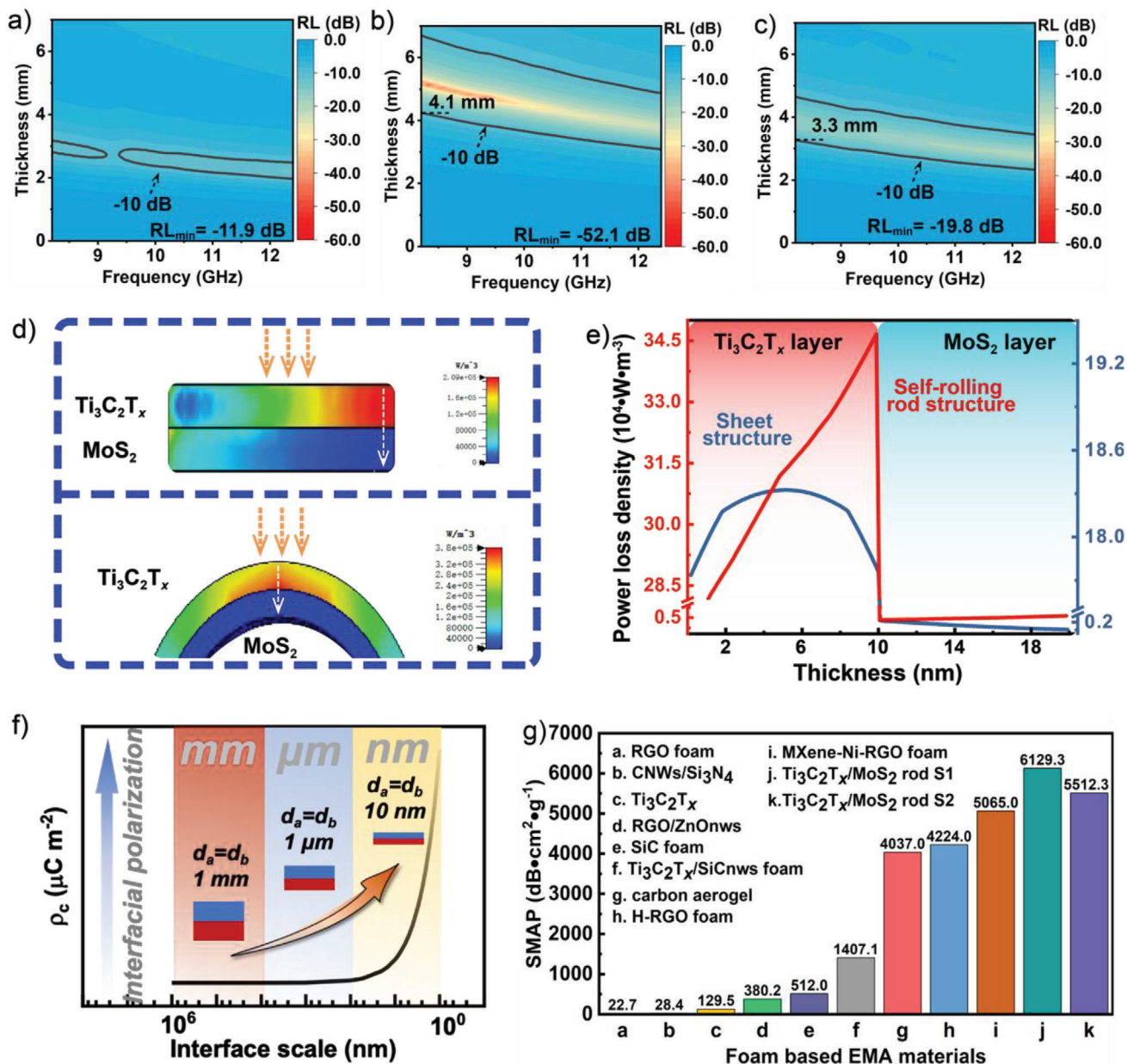


Figure 4. The 2D contours of reflection coefficient versus frequency and thickness (0–7 mm) of a) $\text{Ti}_3\text{C}_2\text{T}_x/\text{MoS}_2$ sheet, b) $\text{Ti}_3\text{C}_2\text{T}_x/\text{MoS}_2$ self-rolling rod S1, and c) $\text{Ti}_3\text{C}_2\text{T}_x/\text{MoS}_2$ self-rolling rod S2. d) The distribution of power loss density of sheet structure and rod structure on the heterogeneous interface. e) The value difference of power loss density for sheet structure and rod structure extracted from the white line. f) The relationship of interface scale and interfacial polarization loss (the abscissa axis is logarithm). g) Comparison of the SMAP of the $\text{Ti}_3\text{C}_2\text{T}_x/\text{MoS}_2$ foams in this work with the reported foam-based EMA materials.

structure models are constructed in the CST microwave studio (Figure S20, Supporting Information). The power loss density (PLD) is used to evaluate the EMA absorption ability in different structures. Two lines passing through the highest values of PLD are chosen as representatives. Compared with sheet structure, the self-rolling rod structure shows higher EMA absorption ability at the heterogeneous interface area (Figure 4e and Figure S18, Supporting Information). Apart from that, the PLD values of the self-rolling rod structure are much higher than the sheet structure, which can lead to better EMA performance. The Maxwell–

Wagner theory also can be used to describe the interfacial polarization loss (Figure S19, Supporting Information).^[29] The intensity of interfacial polarization loss can be expressed by interfacial charge accumulated density $\rho(t)(\mu\text{Cm}^{-2})$ ^[30]

$$\rho(t) = \frac{\epsilon_A \sigma_B - \epsilon_B \sigma_A}{\sigma_A d_B + \sigma_B d_A} U_0 (1 - e^{-\frac{t}{\tau}}) \quad (1)$$

$$\tau = \frac{d_A \epsilon_B + d_B \epsilon_A}{d_A \sigma_B + d_B \sigma_A} \quad (2)$$

where ϵ_A and ϵ_B are permittivity of A phase with low conductivity and B phase with high conductivity, d_A and d_B are the thickness of A and B phases, U_0 is the activation energy and τ is the relaxation time. When $d_A = d_B$, Equation (2) can be simplified to the following equation

$$\tau = \frac{\epsilon_B + \epsilon_A}{\sigma_B + \sigma_A} \quad (3)$$

Higher $\rho(t)$ means stronger interfacial polarization loss. For two certain kinds of materials with similar thickness, the $\rho(t)$ is only related to interfacial thicknesses d_A and d_B . As a result, the thinner the interface, the higher the interfacial polarization loss. For the $\text{Ti}_3\text{C}_2\text{T}_x/\text{MoS}_2$ self-rolling rod structure, the thickness of interfaces was only about 10 nm, which lead to the remarkable improvement of polarization loss. Apart from that, the work functions can affect the accumulation of charges at heterogeneous interfaces, which is related to interfacial polarization loss. The work function difference between $\text{Ti}_3\text{C}_2\text{T}_x$ and few-layer MoS_2 is higher than bulk MoS_2 (Figure S21, Supporting Information), which indicates the interfacial polarization loss of $\text{Ti}_3\text{C}_2\text{T}_x/\text{MoS}_2$ self-rolling rod structure is stronger than sheet structure.^[31] The work function of few-layer MoS_2 is higher than $\text{Ti}_3\text{C}_2\text{T}_x$, which means that the polarized charges will flow to MoS_2 from $\text{Ti}_3\text{C}_2\text{T}_x$. As a result, the ratio of ϵ_p'' is higher than 80%, which surpasses other EMA materials (Table S2, Supporting Information). The high ratio of ϵ_p'' endow our samples with superior EMA performance. For a more comprehensive evaluation, the specific EM absorption performance (SMAP), which includes RL, density, and thickness at the same time, is used to evaluate the performance of our samples. The SMAP of $\text{Ti}_3\text{C}_2\text{T}_x/\text{MoS}_2$ foams is higher than $6100 \text{ dB cm}^2 \text{ g}^{-1}$, due to highly ordered structure and effective interfacial polarization loss after the addition of MoS_2 . Besides, other foam-based EMA materials with EAB at X band are summarized and their corresponding SMAP is shown in Figure 4g and Table S3 in the Supporting Information. The SMAP of $\text{Ti}_3\text{C}_2\text{T}_x/\text{MoS}_2$ self-rolling rod foams is superior to these reported foam-based materials,^[7a,32] demonstrating the advantages of self-rolling rod structures.

3. Conclusions

In this work, the different surface tension directions of ATM and $\text{Ti}_3\text{C}_2\text{T}_x$ derived from the varied hydrophilic properties induce the self-rolling of $\text{Ti}_3\text{C}_2\text{T}_x/\text{MoS}_2$ rod structures. According to the simulation and Maxwell–Wagner theory, interfacial polarization loss significantly increases in self-rolling rod structures. Based on the calculation results of Debye theory, the polarization loss plays a primary role with a ratio of higher than 80% in $\text{Ti}_3\text{C}_2\text{T}_x/\text{MoS}_2$ rod structures. In other words, the interfacial polarization loss is more important than its conduction loss for EMA performance in this system. As a result, the $\text{Ti}_3\text{C}_2\text{T}_x/\text{MoS}_2$ rod structures show better EMA performance compared with $\text{Ti}_3\text{C}_2\text{T}_x/\text{MoS}_2$ sheets, which can realize effective absorption at the whole X band. The SMAP is higher than $6100 \text{ dB cm}^2 \text{ g}^{-1}$ with a density of 0.009 g cm^{-3} . A self-rolling rod structure based on $\text{Ti}_3\text{C}_2\text{T}_x/\text{MoS}_2$ was proposed to realize high interfacial polarization loss for obtaining high-performance EMA materials. This

work provides a new insight to design excellent foam-based EMA materials with self-rolling rod structures.

4. Experimental Section

Preparation of $\text{Ti}_3\text{C}_2\text{T}_x$ MXenes: $\text{Ti}_3\text{C}_2\text{T}_x$ was prepared according to an in situ acid-etching method. Typically, LiF (1 g, Aladdin materials, China) and HCl (10 mL, 9 M, Aladdin materials, China) were mixed. 2 g of Ti_3AlC_2 powder (Jilin 11 technology, China) was added into the mixed solution slowly, following stirring at 40°C for 24 h. Then, the etching products were collected through centrifugation at 3500 rpm until the supernatant became clear. After that, the mixture was washed about ten times with handshaking, until the supernatant became black. The black $\text{Ti}_3\text{C}_2\text{T}_x$ supernatant was collected. The concentration of the suspension was evaluated through the vacuum filtration method.

Preparation of $\text{Ti}_3\text{C}_2\text{T}_x/\text{MoS}_2$ Foam: Firstly, the concentration of the $\text{Ti}_3\text{C}_2\text{T}_x$ suspension was concentrated to 3, 4, and 5 mg mL^{-1} , respectively. Then, 0.03 g ATM (Aladdin materials, China) was added to the above solution and sonicated for 30 min for uniform dispersion. After that, the solution was freeze-dried for 48 h to form the porous structure.^[33] Finally, the as-prepared foams were calcined for 2 h at 350°C under 90% Ar and 10% H_2 . The samples were named S1, S2, and S3, corresponding to the concentration of 3, 4, and 5 mg mL^{-1} , respectively. The pure $\text{Ti}_3\text{C}_2\text{T}_x$ foam was 5 mg mL^{-1} . The $\text{Ti}_3\text{C}_2\text{T}_x/\text{MoS}_2$ foams composed of $\text{Ti}_3\text{C}_2\text{T}_x/\text{MoS}_2$ sheets were also prepared. Typically, the ATM were annealed at first and then mixed with $\text{Ti}_3\text{C}_2\text{T}_x$ suspension of 5 mg mL^{-1} , followed by the same unidirectional freezing and annealing processes.

Microstructure Characterization: The structures of foams were characterized by tabletop microscopes (TM400plus, Hitachi, Japan). The morphology of the $\text{Ti}_3\text{C}_2\text{T}_x/\text{MoS}_2$ rod was characterized by SEM (Sigma 300, Zeiss, Germany). The preparation TEM sample through FIB proceeded on FIB (Helios G4 CX, FEI, USA). The distribution of MoS_2 on the $\text{Ti}_3\text{C}_2\text{T}_x$ sheets was observed by Double Cs Corrector TEM (Themis Z, FEI, USA). XRD (D8 Advance, Bruker, Germany) and Raman (He-Ne laser, $\lambda = 532 \text{ nm}$ Renishaw, UK) were exploited to analyze the phase compositions. The chemical bonds were characterized by XPS (K-Alpha, Waltham, Thermo Scientific, USA). TG curves of ATM were obtained on simultaneous thermal analysis (STA 449F3, Netzsch, Germany) in the temperature range of $30\text{--}400^\circ\text{C}$ under Ar.

Measurement and Calculation of EMA Performance: The S-parameters and permittivity of the final foams were obtained through the wave-guide method (ASTM D5568-14) at a frequency range of 8.2–12.4 GHz. Based on the permittivity, the RL (dB) was obtained through the following equations

$$Z_{\text{in}} = \sqrt{\frac{\mu}{\epsilon}} \tanh \left[j \left(\frac{2\pi f d}{c} \right) \sqrt{\mu\epsilon} \right] \quad (4)$$

$$\text{RL} = 20 \log_{10} \left| \frac{Z_{\text{in}} - 1}{Z_{\text{in}} + 1} \right| \quad (5)$$

where Z_{in} is the normalized impedance, and μ, ϵ, c, f , and d are permeability, permittivity, speed of light in vacuum, frequency of the EM wave, and the thickness of the test samples. The corresponding frequency range of RL lower than -10 dB is called EAB. The SMAP is adopted as one evaluation index, integrating with density, thickness, RL values, and effective bandwidth. The SMAP values are calculated by the following equation

$$\text{SMAP}(\text{dBcm}^2 \text{g}^{-1}) = \frac{\int_{f_a}^{f_b} \text{RL} df}{f_b - f_a} / (\rho \cdot d) \quad (6)$$

where f_a is the start frequency (8.2 GHz) and f_b is the stop frequency (12.4 GHz), d is the thickness, and ρ is the bulk density of the foam.

Supporting Information

Supporting Information is available from the Wiley Online Library or from the author.

Acknowledgements

This work was financially supported by the National Science and Technology Major Project (Grant No. J2019-VI-0014-0129) and the National Natural Science Foundation of China (Grant Nos. 52072303 and 51821091). The authors would like to thank the Analytical and Testing Center of Northwestern Polytechnical University for the SEM and TEM images. The authors would like to give their special thanks to Prof. Xiaowei Yin for his kind guidance and help on the research work.

Conflict of Interest

The authors declare no conflict of interest.

Data Availability Statement

Research data are not shared.

Keywords

electromagnetic wave absorption, heterogeneous interfaces, MoS₂, MXene foams, self-rolling rod

Received: February 25, 2022

Revised: March 15, 2022

Published online: April 11, 2022

- [1] a) Q. Song, F. Ye, L. Kong, Q. Shen, L. Han, L. Feng, G. Yu, Y. Pan, H. Li, *Adv. Funct. Mater.* **2020**, *30*, 2000475. b) H. Chen, W. Ma, Z. Huang, Y. Zhang, Y. Huang, Y. Chen, *Adv. Opt. Mater.* **2019**, *7*, 1801318. c) R. Qiang, Y. Du, Y. Wang, N. Wang, C. Tian, J. Ma, P. Xu, X. Han, *Carbon* **2016**, *98*, 599. d) D. Ding, Y. Wang, X. Li, R. Qiang, P. Xu, W. Chu, X. Han, Y. Du, *Carbon* **2017**, *111*, 722. e) M. Li, X. Yin, H. Xu, X. Li, L. Cheng, L. Zhang, *J. Am. Ceram. Soc.* **2019**, *102*, 5305. f) H. Sun, R. Che, X. You, Y. Jiang, Z. Yang, J. Deng, L. Qiu, H. Peng, *Adv. Mater.* **2014**, *26*, 8120. g) M. Li, X. Fan, H. Xu, F. Ye, J. Xue, X. Li, L. Cheng, *J. Mater. Sci. Technol.* **2020**, *59*, 164. h) X. Fang, L. Jiang, L. Pan, S. Yin, T. Qiu, J. Yang, *J. Adv. Ceram.* **2021**, *10*, 301.
- [2] a) M. Qin, L. Zhang, H. Wu, *Adv. Sci.* **2022**, <https://doi.org/10.1002/advs.202105553>. b) B. Quan, W. Shi, S. J. H. Ong, X. Lu, P. L. Wang, G. Ji, Y. Guo, L. Zheng, Z. J. Xu, *Adv. Funct. Mater.* **2019**, *29*, 1901236.
- [3] a) L. Liang, W. Gu, Y. Wu, B. Zhang, G. Wang, Y. Yang, G. Ji, *Adv. Mater.* **2022**, *34*, 2106195. b) X. Yang, B. Fan, X. Tang, J. Wang, G. Tong, D. Chen, J. Guan, *Chem. Eng. J.* **2022**, *430*, 132747.
- [4] a) M. Naguib, M. Kurtoglu, V. Presser, J. Lu, J. Niu, M. Heon, L. Hultman, Y. Gogotsi, M. W. Barsoum, *Adv. Mater.* **2011**, *23*, 4248. b) M. Naguib, V. N. Mochalin, M. W. Barsoum, Y. Gogotsi, *Adv. Mater.* **2014**, *26*, 992. c) M. Alhabeab, K. Maleski, B. Anasori, P. Lelyukh, L. Clark, S. Sin, Y. Gogotsi, *Chem. Mater.* **2017**, *29*, 7633. d) X. Fan, M. Li, X. Li, F. Ye, J. Xue, L. Zhang, L. Cheng, *Chin. Chem. Lett.* **2020**, *31*, 1026. e) Z. Fan, D. Wang, Y. Yuan, Y. Wang, Z. Cheng, Y. Liu, Z. Xie, *Chem. Eng. J.* **2020**, *381*, 122696. f) F. Shahzad, M. Alhabeab, C. B. Hatter, B. Anasori, S. Man Hong, C. M. Koo, Y. Gogotsi, *Science* **2016**, *353*, 1137.
- [5] a) M. Han, Y. Liu, R. Rakhmanov, C. Israel, M. A. S. Tajin, G. Friedman, V. Volman, A. Hoorfar, K. R. Dandekar, Y. Gogotsi, *Adv. Mater.* **2021**, *33*, 2003225. b) M. Han, C. E. Shuck, R. Rakhmanov, D. Parchment, B. Anasori, C. M. Koo, G. Friedman, Y. Gogotsi, *ACS Nano* **2020**, *14*, 5008.
- [6] M. Han, X. Yin, K. Hantanasirisakul, X. Li, A. Iqbal, C. B. Hatter, B. Anasori, C. M. Koo, T. Torita, Y. Soda, L. Zhang, L. Cheng, Y. Gogotsi, *Adv. Opt. Mater.* **2019**, *7*, 1900267.
- [7] a) X. Li, X. Yin, H. Xu, M. Han, M. Li, S. Liang, L. Cheng, L. Zhang, *ACS Appl. Mater. Interfaces* **2018**, *10*, 34524. b) T. Hou, B. Wang, M. Ma, A. Feng, Z. Huang, Y. Zhang, Z. Jia, G. Tan, H. Cao, G. Wu, *Composites, Part B* **2020**, *180*, 107577.
- [8] J. Wang, L. Liu, S. Jiao, K. Ma, J. Lv, J. Yang, *Adv. Funct. Mater.* **2020**, *30*, 2002595.
- [9] a) X. Li, M. Li, X. Lu, W. Zhu, H. Xu, J. Xue, F. Ye, Y. Liu, X. Fan, L. Cheng, *Chem. Eng. J.* **2021**, *419*, 129414. b) Z. Hou, J. Xue, H. Wei, X. Fan, F. Ye, S. Fan, L. Cheng, L. Zhang, *Ceram. Int.* **2020**, *46*, 18160. c) H. Wang, H. Wu, H. Pang, Y. Xiong, S. Ma, Y. Duan, Y. Hou, C. Mao, *J. Mater. Sci. Technol.* **2022**, *97*, 213. d) X. Yang, Y. Duan, S. Li, L. Huang, H. Pang, B. Ma, T. Wang, *Carbon* **2022**, *188*, 376. e) X. Zhang, Y. Shi, J. Xu, Q. Ouyang, X. Zhang, C. Zhu, X. Zhang, Y. Chen, *Nano-Micro Lett.* **2022**, *14*, 27.
- [10] a) N. Lavoine, L. Bergström, *J. Mater. Chem. A* **2017**, *5*, 16105. b) N. T. Cervin, E. Johansson, J. W. Benjamins, L. Wagberg, *Biomacromolecules* **2015**, *16*, 822.
- [11] a) N. Denkov, S. Tcholakova, I. Lesov, D. Cholakova, S. K. Smoukov, *Nature* **2015**, *528*, 392. b) Z. Chen, W. Yang, B. Xu, Y. Guo, Y. Chen, X. Yin, Y. Liu, *Prog. Org. Coat.* **2018**, *122*, 159.
- [12] Y. Deng, T. Shang, Z. Wu, Y. Tao, C. Luo, J. Liang, D. Han, R. Lyu, C. Qi, W. Lv, F. Kang, Q. H. Yang, *Adv. Mater.* **2019**, *31*, 1902432.
- [13] M. Nath, A. Govindaraj, C. N. R. Rao, *Adv. Mater.* **2001**, *13*, 283.
- [14] M. Ning, M. Lu, J. Li, Z. Chen, Y. Dou, C. Wang, F. Rehman, M. Cao, H. Jin, *Nanoscale* **2015**, *7*, 15734.
- [15] L. Ding, Y. Wei, Y. Wang, H. Chen, J. Caro, H. Wang, *Angew. Chem., Int. Ed.* **2017**, *129*, 1851.
- [16] M. Han, X. Yin, X. Li, B. Anasori, L. Zhang, L. Cheng, Y. Gogotsi, *ACS Appl. Mater. Interfaces* **2017**, *9*, 20038.
- [17] J. Liu, Y. Liu, D. Xu, Y. Zhu, W. Peng, Y. Li, F. Zhang, X. Fan, *Appl. Catal. B* **2018**, *241*, 89.
- [18] J. Xu, M. Liu, X. Zhang, B. Li, X. Zhang, X. Zhang, C. Zhu, Y. Chen, *Appl. Phys. Rev.* **2022**, *9*, 011402.
- [19] T. Shang, Z. Lin, C. Qi, X. Liu, P. Li, Y. Tao, Z. Wu, D. Li, P. Simon, Q. Yang, *Adv. Funct. Mater.* **2019**, *29*, 1903960.
- [20] a) Y. Li, Z. Yin, G. Ji, Z. Liang, Y. Xue, Y. Guo, J. Tian, X. Wang, H. Cui, *Appl. Catal. B* **2019**, *246*, 12. b) D. K. Nandi, S. Sahoo, S. Sinha, S. Yeo, H. Kim, R. N. Bulakhe, J. Heo, J. J. Shim, S. H. Kim, *ACS Appl. Mater. Interfaces* **2017**, *9*, 40252. c) Q. Q. Xiong, Z. G. Ji, *J. Alloys Compd.* **2016**, *673*, 215.
- [21] a) G. Yang, Z. Yan, T. Xiao, *Appl. Surf. Sci.* **2012**, *258*, 4016. b) F. Wei, L. Ni, P. Cui, *J. Hazard. Mater.* **2008**, *156*, 135. c) C. Duret-Thual, D. Costa, W. P. Yang, P. Marcus, *Corros. Sci.* **1997**, *39*, 913.
- [22] a) Z. Hu, X. Kuai, J. Chen, P. Sun, Q. Zhang, H. Wu, L. Zhang, *ChemSusChem* **2020**, *13*, 1485. b) N. Scheuschner, R. Gillen, M. Staiger, J. Maultzsch, *Phys. Rev. B* **2015**, *91*, 235409. c) K. M. Price, S. Najmaei, C. E. Ekuma, R. A. Burke, M. Dubey, A. D. Franklin, *ACS Appl. Nano Mater.* **2019**, *2*, 4085.
- [23] L. Zhan, W. Wan, Z. Zhu, T. Shih, W. Cai, *J. Phys.: Conf. Ser.* **2017**, *864*, 012037.
- [24] H. Li, Q. Zhang, C. C. R. Yap, B. K. Tay, T. H. T. Edwin, A. Olivier, D. Baillargeat, *Adv. Funct. Mater.* **2012**, *22*, 1385.
- [25] a) L. Cheng, J. Lee, H. Zhu, A. V. Ravichandran, Q. Wang, A. T. Lucero, M. J. Kim, R. M. Wallace, L. Colombo, J. Kim, *ACS Nano* **2017**, *11*, 10243. b) Y. Shi, J. Wang, C. Wang, T. Zhai, W. Bao, J. Xu, X. Xia, H. Chen, *J. Am. Chem. Soc.* **2015**, *137*, 7365.

- [26] L. A. Giannuzzi, F. A. Stevie, *Micron* **1999**, *30*, 197.
- [27] H. Liang, H. Xing, Z. Ma, H. Wu, *Carbon* **2021**, *183*, 138.
- [28] X. Zhou, Z. Jia, X. Zhang, B. Wang, W. Wu, X. Liu, B. Xu, G. Wu, *J. Mater. Sci. Technol.* **2021**, *87*, 120.
- [29] a) D. Guo, H. Yuan, X. Wang, C. Zhu, Y. Chen, *ACS Appl. Mater. Interfaces* **2020**, *12*, 9628. b) Q. Li, Y. Zhao, X. Li, L. Wang, X. Li, J. Zhang, R. Che, *Small* **2020**, *16*, 2003905. c) C. Han, M. Zhang, W. Cao, M. Cao, *Carbon* **2021**, *171*, 953. d) W. Ma, P. He, T. Wang, J. Xu, X. Liu, Q. Zhuang, Z. Cui, S. Lin, *Chem. Eng. J.* **2021**, *420*, 129875.
- [30] F. Rogti, M. Ferhat, *J. Electrostat.* **2014**, *72*, 91.
- [31] a) L. Britnell, R. M. Ribeiro, A. Eckmann, R. Jalil, B. D. Belle, A. Mishchenko, Y.-J. Kim, R. V. Gorbachev, T. Georgiou, S. V. Morozov, A. N. Grigorenko, A. K. Geim, C. Casiraghi, A. H. C. Neto, K. S. Novoselov, *Science* **2013**, *340*, 1311. b) X. Xu, T. Guo, M. K. Hota, H. Kim, D. Zheng, C. Liu, M. N. Hedhili, R. S. Alsaadi, X. Zhang, H. N. Alshareef, *Adv. Mater.* **2021**, <https://doi.org/10.1002/adma.202107370>. c) M. j. Velický, M. A. Bissett, C. R. Woods, P. S. Toth, T. Georgiou, I. A. Kinloch, K. S. Novoselov, R. A. Dryfe, *Nano Lett.* **2016**, *16*, 2023.
- [32] a) K. Hu, H. Wang, X. Zhang, H. Huang, T. Qiu, Y. Wang, C. Zhang, L. Pan, J. Yang, *Chem. Eng. J.* **2020**, *408*, 127283. b) C. Song, X. Yin, M. Han, X. Li, Z. Hou, L. Zhang, L. Cheng, *Carbon* **2017**, *116*, 50. c) L. Liang, Q. Li, X. Yan, Y. Feng, Y. Wang, H. B. Zhang, X. Zhou, C. Liu, C. Shen, X. Xie, *ACS Nano* **2021**, *15*, 6622. d) M. Zhang, X. Fang, Y. Zhang, J. Guo, C. Gong, D. Estevez, F. Qin, J. Zhang, *Nanotechnology* **2020**, *31*, 275707.
- [33] J. Xu, X. Zhang, Z. Zhao, H. Hu, B. Li, C. Zhu, X. Zhang, Y. Chen, *Small* **2021**, *17*, 2102032.